C103-E134

SHIMADZU
Excellence in Science

FTIR
TALK LETTER
Vol. 37

Development of Heterogeneous Catalytic Systems Based on Crystalline Mixed Oxides and the Mechanism of Molecule Activation on a Solid Catalyst Surface Using FTIR Spectroscopy

Laboratory for Materials and Structures, Institute of Innovative Research, Tokyo Institute of Technology
Keigo Kamata, Associate Professor

1. Introduction

Mixed oxides are an important group of inorganic compounds used in a wide range of applications related to semiconductors, piezoelectric materials, electronic materials, and magnetic materials due to the electronic and magnetic properties originating from their unique structure. In the field of catalysis, recent advances not only in synthesis and measurement technology but also in theoretical computation have led to the excellent catalytic properties of mixed oxides as acid-base and redox catalysts. Compared to homogeneous metal complexes and organocatalysts, the design and precise synthesis of mixed oxide solid catalysts to achieve the desired reaction remain challenging subjects of research. However, detailed reaction mechanism of solid catalysts including the activation mode of substrates and reactants and the structure-activity relationship remains unclear. These problems make it difficult to design and synthesize highly functionalized solid catalysts.

Against such a background, our research group has proposed new concepts and methodologies for the design of high-performance catalysts based on polyoxometalates, anionic metal oxygen cluster molecules. We have developed environmentally friendly and practical reaction systems with these polyoxometalate catalysts.[1] Based on the findings and concepts that emerged in our study of polyoxometalates, we have also started developing new solid catalysts, such as perovskite oxides and metal phosphates for oxidation reactions with molecular oxygen (O_2) as the sole oxidant and bifunctional acid-base catalysis, respectively (Fig. 1).[2]-[9] This article describes oxidation catalysis and acid-base catalysis by these two types of solid materials and the mechanistic studies on molecule activation using FTIR spectroscopy.

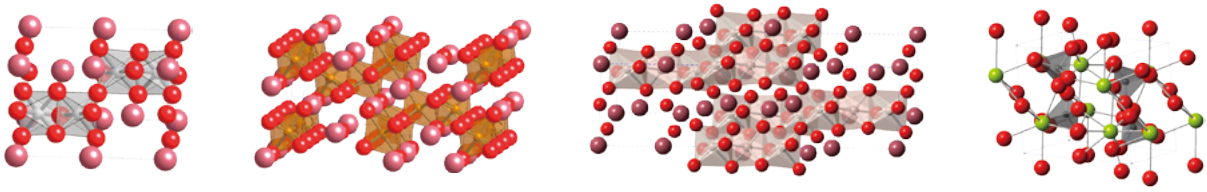

$SrMnO_3$ $BaFeO_{3-\delta}$ $BaRuO_3$ $CePO_4$

Fig. 1 Crystal Structure of Perovskite Oxides ($SrMnO_3$, $BaFeO_{3-\delta}$ and $BaRuO_3$) and a Metal Phosphate ($CePO_4$)

2. Oxidation Reactions with Perovskite Oxides

Selective oxidation reactions account for 30 % of all chemical processes and play an important role in chemical industry to convert various petroleum-based feedstocks into useful oxidation products. Despite the merits of using molecular oxygen (O_2) as the sole oxidant, examples of heterogeneous oxidation catalysts, that are applicable to a wide range of substrates and can activate O_2 under mild conditions, are still limited. We found that hexagonal $SrMnO_3$, a perovskite catalyst synthesized by a polymerized complex method, functions as an efficient heterogeneous catalyst for the selective oxidation of various substrates with O_2.[7] From the catalyst effects of various Mn compounds on oxidation of 1-phenylethanol with O_2,

$SrMnO_3$ gave higher yield of acetophenone (83 %) than activated MnO_2 (59 %) even with a larger surface area (122 $m^2\ g^{-1}$) than $SrMnO_3$ (25 $m^2\ g^{-1}$). Other Mn^{2+} and Mn^{3+} containing oxides and complexes were inactive under the same reaction conditions (1 to 6 % yield). The hot-filtration experiments suggested that this reaction occurred on the solid surface. In addition, the catalyst recovered by filtration could be reused with no loss of activity. The $SrMnO_3$ catalyst was applicable to the oxidation of primary and secondary benzylic and allylic alcohols with O_2 to the corresponding carbonyl compounds. We investigated the reaction mechanism for alcohol oxidation by the $SrMnO_3$ catalyst (Fig. 2). In the case of MnO_2 where lattice oxygen contributes to the reaction, oxidation occurs in both an O_2 and Ar atmosphere. On the other hand, oxidation with $SrMnO_3$ was promoted significantly by the presence of O_2, suggesting an O_2-activation mechanism (Fig. 2(a)). Accordingly, we measured the O_2-adsorbed IR spectrum to detect surface active oxygen species (Fig. 2(b)). When $^{16}O_2$ was exposed at room temperature to $SrMnO_3$ pretreated under vacuum at 300 °C, a new absorption band appeared at 1152 cm^{-1} and the band position is similar to the reported values (from 1200 to 1100 cm^{-1}) for ν(O-O) bands of metal-superoxo species. This absorption band disappeared after evacuation and was not observed in the case of MnO_2. The IR spectrum of $SrMnO_3$ with adsorbed $^{18}O_2$ under similar conditions showed an absorption band at 1086 cm^{-1} with an isotope shift that is consistent with theoretical values. Although the isolation of Mn-superoxo complexes and theoretical studies of O_2 reduction on $La_{1-x}Sr_xMnO_3$ have been reported, there are no reports of O_2 reductive activation on $SrMnO_3$ and its catalytic applications. Based on the above-described investigation with FTIR and kinetic analysis, we proposed that reversibly generated Mn-superoxo species play an important role in this oxidation reaction (Fig. 2(c)).

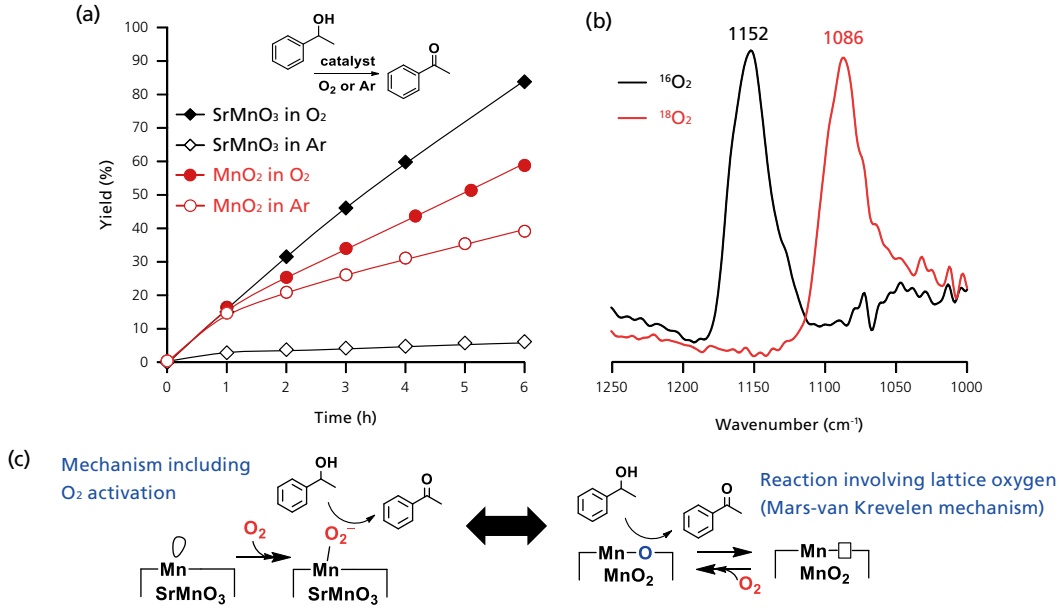

Fig. 2 (a) Time course of 1-phenylethanol oxidation by O_2 using Mn oxides
(b) IR spectra of $SrMnO_3$ adsorbed with $^{16}O_2$ and $^{18}O_2$
(c) Proposed mechanism of alcohol oxidation by Mn oxides

The polymerized complex methods have disadvantages such as multi-step synthesis and applicability; thus, we focused on the importance of amorphous precursor formation in perovskite nanoparticle synthesis and developed a simple and efficient new synthesis route using an amino acid (aspartic acid).[2]-[6] Hexagonal $SrMnO_3$ with a high surface area (up to 50 $m^2\ g^{-1}$) was successfully synthesized by low-temperature calcination of an amorphous precursor prepared using aspartic acid and metal acetates. These $SrMnO_3$ nanoparticles exhibited much higher catalytic performance than a sample synthesized by the polymerized complex method. This synthesis method can be applied to various combinations of elements, resulting in the synthesis of various nano-sized perovskite oxides such as hexagonal 6H-$BaFeO_{3-\delta}$ with high-valent iron and rhombohedral $BaRuO_3$. Hexagonal 6H-$BaFeO_{3-\delta}$ functioned as an efficient and reusable solid catalyst in the oxidation of adamantane and various alkanes at ambient pressures of O_2 as the only oxidant as well as in the oxidative cleavage of carbon-carbon double bonds in alkenes.[3] [4] This is the first reported example of a solid catalyst based on a naturally abundant iron oxide that catalyzes the additive-free oxidation of adamantane with only O_2. Rhombohedral $BaRuO_3$ also functioned as an efficient heterogeneous catalyst in the selective oxidation of various aromatics and aliphatic sulfides using only O_2.[5]

3. Acid-Base Reactions with Metal Phosphates

Concerted activation of substrates by multiple active sites with acid-base properties can result in specific catalytic activity and selectivity. However, difficulty in the construction of uniform and structurally controlled acid-base sites on solid materials often leads to a problem where the fine-tuning of the catalyst structure and the reactivity are restrained. Accordingly, the design and development of new and highly active acid-base inorganic solid catalysts is an important topic of study. We anticipated that rare-earth orthophosphates would be good candidates as bifunctional acid-base catalysts that can work in concert to promote electrophilicity and nucleophilicity in reactive partners. This section describes the highly chemoselective acetalization of carbonyl compounds by a monoclinic $CePO_4$ catalyst synthesized using the hydrothermal method and the investigation on the acid-base properties using FTIR spectroscopy for samples with adsorbed probe molecules.[8]

Monoclinic $CePO_4$ was synthesized by the reaction of $Ce(NO_3)_3$ and $(NH_4)_2HPO_4$ under hydrothermal conditions. The scanning electron microscope measurement for $CePO_4$ revealed the formation of nano-sized rod like shaped particles. 5-Hydroxymethylfurfural (HMF), a compound derived from sugars with alcohol and aldehyde functionalities, was acetalized with methanol in the presence of various acid-base catalysts. Among the catalysts tested, $CePO_4$ was the most effective for the acetalization to give the corresponding acetal in 78 % yield with a selectivity of 96 %. The reaction did not proceed in the absence of a catalyst, and homogeneous acid catalysts and base catalysts were inactive in chemoselective acetalization of HMF. We also examined metal oxides previously reported to function as efficient acid-base catalysts. Nb_2O_5 was not as effective as $CePO_4$ in catalyzing the acetalization reaction and other metal oxides (SiO_2, ZrO_2, CeO_2, Al_2O_3, MgO, TiO_2, and SnO_2) were almost inactive. Typical solid acid catalysts gave a complex mixture of products, and a mixture of catalyst precursors was not effective. In the presence of $CePO_4$, various combinations of carbonyl compounds and alcohols were converted into their corresponding acetal compounds with high yields (Fig. 3). The present catalytic system was applicable to large-scale acetalization of HMF with methanol and regioselective synthesis of solketal from acetone and glycerol.

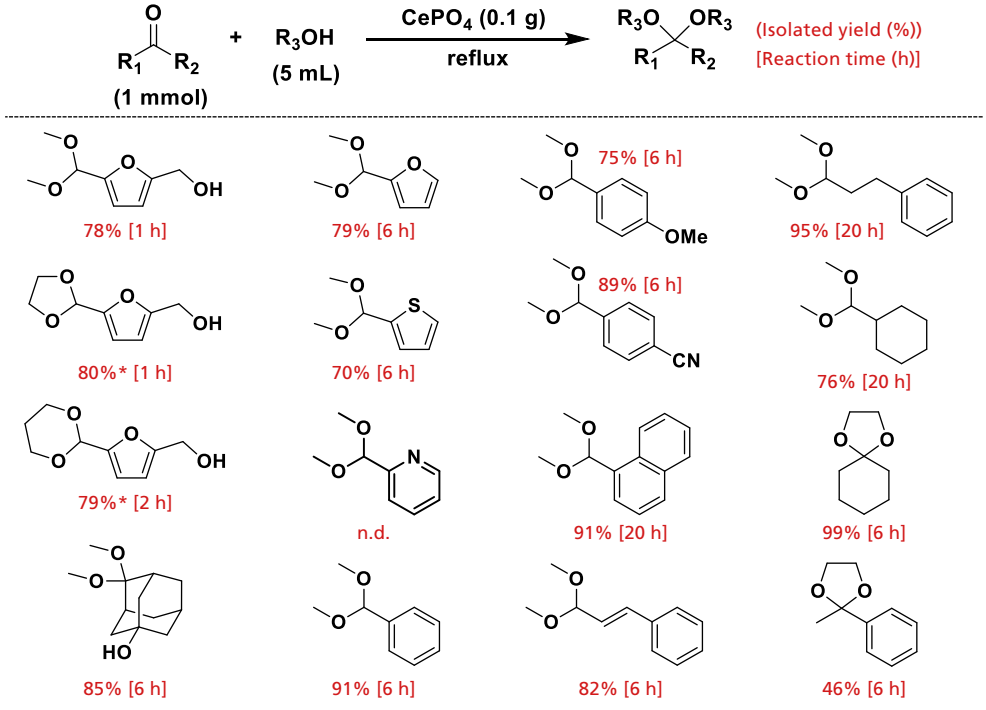

Fig. 3 Acetalization of Various Substrates with $CePO_4$ Catalyst

The acid properties of $CePO_4$ were evaluated by IR spectroscopy for a sample adsorbed with pyridine as a probe molecule (Fig. 4(a)). The IR spectrum of $CePO_4$ with adsorbed pyridine revealed an absorption band at 1445 cm^{-1} associated with a pyridine species coordinated to a Lewis acid site and no absorption band at 1540 cm^{-1} associated with a pyridinium ion bound to a Brønsted acid site. Based on absorption band intensity, the amount of Lewis acid sites on $CePO_4$ was estimated to be 0.096

mmol g^{-1}. The IR spectrum of $CePO_4$ with adsorbed chloroform showed a red-shift in the chloroform molecule ν(C-H) absorption band from 3034 cm^{-1} to 3008 cm^{-1}, which suggests the presence of surface base sites (Fig. 4(b)). A new absorption band also appeared at 1250 cm^{-1} associated with δ(Cl-C-H) in the chloroform molecule caused by simultaneous interaction with acid sites and base sites. These results show base sites on $CePO_4$ are located close to Lewis acid sites, which is in good agreement with the crystal structure of $CePO_4$.

Although CeO_2 is also known to function as an efficient acid-base catalyst, only $CePO_4$ was effective for chemoselective acetalization of HMF; thus, the substrate activation modes of $CePO_4$ and CeO_2 were investigated using IR measurements for samples with adsorbed acetone and methanol. A strong absorption band (1699 cm^{-1}) associated with acetone ν(C=O) adsorbed on $CePO_4$ was observed at a lower wavenumber than in gaseous acetone (1731 cm^{-1}) (Fig. 4(c)). In contrast, the IR spectrum of acetone adsorbed to CeO_2 revealed absorption bands associated with the acetone molecule located at different acid sites (1700 cm^{-1} and 1673 cm^{-1}) and absorption bands associated with aldol condensation products (1627 cm^{-1} and 1570 to 1550 cm^{-1}) (Fig. 4(d)). These results indicate the interaction between the uniform Lewis acid sites on $CePO_4$ and the carbonyl oxygen in acetone without the promotion of aldol condensation reaction.

In the regions of ν(O-H) for the IR spectrum of $CePO_4$ with adsorbed methanol, a broad absorption band appeared at 3000 to 3500 cm^{-1} with negative OH absorption. In addition, absorption bands were observed at 2952 and 2849 cm^{-1} associated with $\nu_{as}(CH_3)$ and $\nu_s(CH_3)$, respectively (Fig. 4(e)). This broad absorption band and the absorption band associated with $\nu(CH_3)$ suggest that methanol was molecularly absorbed on $CePO_4$ via hydrogen bonds. In contrast, the IR spectrum of methanol adsorbed to CeO_2 revealed absorption bands at 2911 and 2805 cm^{-1} associated with methoxide species $\nu_{as}(CH_3)$ and $\nu_s(CH_3)$, respectively (Fig. 4(f)). These results indicate that $CePO_4$ functions as a bifunctional catalyst with uniform Lewis acid sites and weak base sites that interact with HMF and methanol, respectively, which results in a highly efficient and chemoselective acetalization reaction.

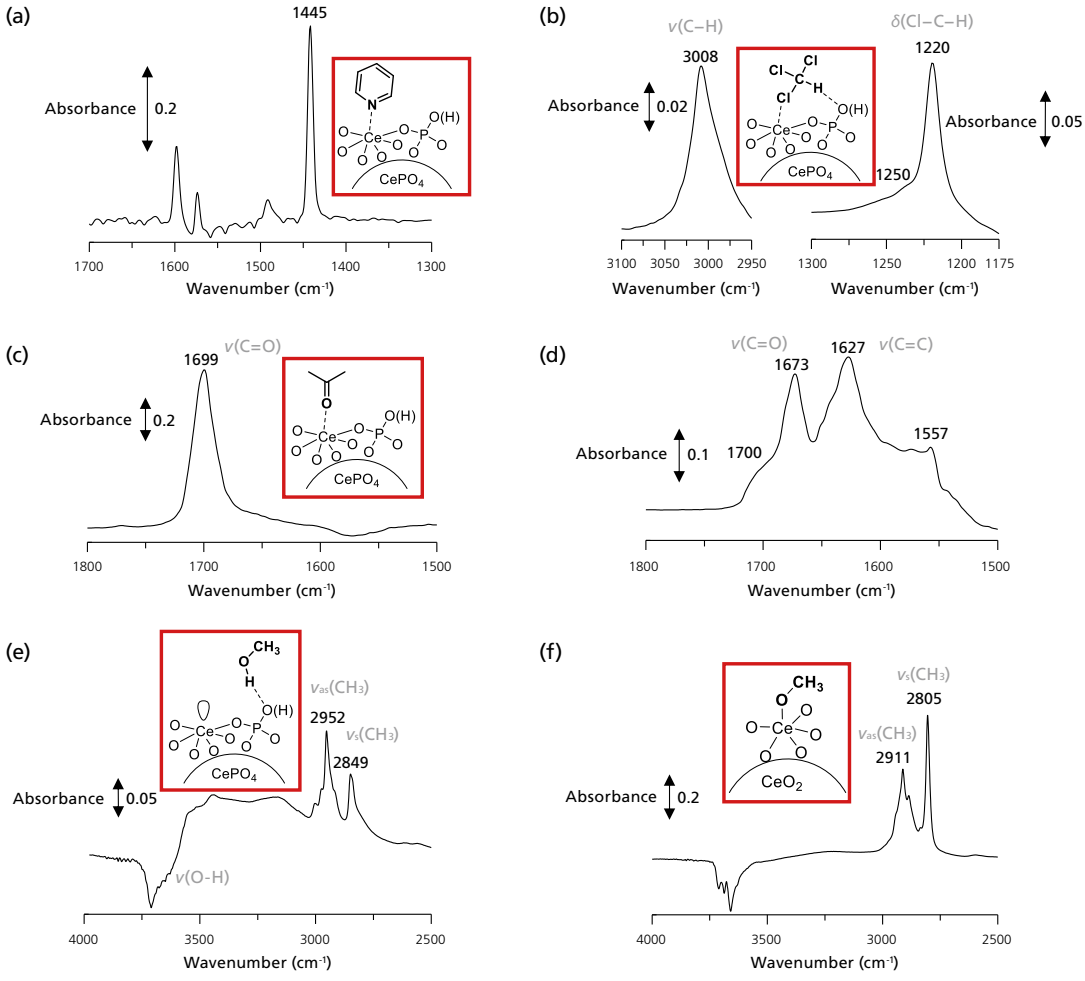

Fig. 4 IR Spectra of (a) Pyridine, (b) Chloroform, (c) Acetone, and (e) Methanol Adsorbed to $CePO_4$. IR Spectra of (d) Acetone and (f) Methanol Adsorbed to CeO_2.

4. Summary

By focusing on the unique structures of crystalline mixed oxides, we developed hexagonal perovskite oxides with face-sharing octahedral units effective for O_2 oxidation and a bifunctional metal phosphate with uniform Lewis acid and weak-base sites. We also confirmed that the FTIR measurements are extremely effective not only to investigate mechanisms of molecule activation on a solid surface but also to reveal the structure-activity relationship. These findings are also applicable to the development and nanostructure control of effective solid catalyst materials such as β-MnO_2 with low oxygen vacancy formation energy.[10]-[13] In addition, our nanomaterials can be applied to catalytic reactions using electrical fields and electrochemical energy.[9], [14]-[16] Further high functionalization (nanoparticle synthesis, morphology control, orientation control, etc.) of these mixed oxides and/or creation of new materials through computational approaches (material informatics, etc.) can lead to the development of innovative catalyst systems to establish difficult "dream reactions" for catalyst researchers.

The above research was performed by using the research facilities of the Laboratory for Materials and Structures (Professor Michikazu Hara Laboratory) at the Institute of Innovative Research, Tokyo Institute of Technology. First-principle calculations were performed by Professor Fumiyasu Oba and Associate Professor Yu Kumagai of the same laboratory. We are also sincerely grateful to all members of our laboratory and other collaborating researchers (Professor Yasushi Sekine and Associate Professor Shuhei Ogo of Waseda University, and Professor Takeo Yamaguchi and Assistant Professor Yuuki Sugawara of Tokyo Institute of Technology) for their guidance and cooperation with this research.

References

[1] K. Kamata, *Bull. Chem. Soc. Jpn.* **2015**, *88*, 1017–1028.
[2] K. Kamata, Bull. *Chem. Soc. Jpn.* **2019**, *92*, 133–151.
[3] S. Shibata, K. Kamata, M. Hara, *Catal. Sci. Technol.* **2021**, *11*, 2369–2373.
[4] S. Shibata, K. Sugahara, K. Kamata, M. Hara, *Chem. Commun.* **2018**, *54*, 6772–6775.
[5] K. Kamata, K. Sugahara, Y. Kato, S. Muratsugu, Y. Kumagai, F. Oba, M. Hara, *ACS Appl. Mater. Interfaces* **2018**, *10*, 23792–23801.
[6] K. Sugahara, K. Kamata, S. Muratsugu, M. Hara, *ACS Omega* **2017**, *2*, 1608–1616.
[7] S. Kawasaki, K. Kamata, M. Hara, *ChemCatChem* **2016**, *8*, 3247–3253.
[8] S. Kanai, I. Nagahara, Y. Kita, K. Kamata, M. Hara, *Chem. Sci.* **2017**, *8*, 3146–3153.
[9] A. Sato, S. Ogo, K. Kamata, Y. Takeno, T. Yabe, T. Yamamoto, S. Matsumura, M. Hara, Y. Sekine, *Chem. Commun.* **2019**, *55*, 4019–4022.
[10] Y. Yamaguchi, R. Aono, E. Hayashi, K. Kamata, M. Hara, *ACS Appl. Mater. Interfaces* **2020**, *12*, 36004–36013.
[11] E. Hayashi, Y. Yamaguchi, Y. Kita, K. Kamata, M. Hara, *Chem. Commun*. **2020**, *56*, 2095–2098.
[12] E. Hayashi, Y. Yamaguchi, K. Kamata, N. Tsunoda, Y. Kumagai, F. Oba, M. Hara, *J. Am. Chem. Soc*. **2019**, *141*, 890–900.
[13] E. Hayashi, T. Komanoya, K. Kamata, M. Hara, *ChemSusChem* **2017**, *10*, 654–658.
[14] Y. Sugawara, K. Kamata, A. Ishikawa, Y. Tateyama, T. Yamaguchi, ACS *Appl. Energy Mater.* **2021**, *4*, 3057–3066.
[15] Y. Sugawara, T. Hihara, G. M. Anilkumar, K. Kamata, T. Yamaguchi, *Sustain. Energy Fuels* **2021**, *5*, 1374–1378.
[16] Y. Sugawara, K. Kamata, T. Yamaguchi, *ACS Appl. Energy Mater.* **2019**, *2*, 956–960.

Optical Systems in Infrared Microscopes

Spectroscopy Business Unit, Analytical & Measuring Instruments Division
Atsuhiko Otaguro

Infrared (IR) microscopes combine the function of an optical microscope that observes the microscopic domain with an IR spectrometer for IR spectroscopy, and switch between viewing microscopic samples in visible light and measuring IR spectra in IR light. This article uses the Shimadzu AIM-9000 IR microscope as an example in describing optical systems in IR microscopes.

1. Introduction

With consumers' recent interest in foreign contaminants, small foreign objects have become an increasingly prevalent issue. Foreign objects large enough to be visible to the eye can probably be analyzed with a single-reflex attenuated total reflectance (ATR) accessory, a common accessory for FTIR, but foreign objects 100 µm or smaller must be analyzed with an IR microscope equipped with a highly sensitive mercury cadmium telluride (MCT) detector.

2. The Optical System of the AIM-9000 IR Microscope

An external view of the AIM-9000 is shown in Fig. 1 and its optical system is shown in Fig. 2. The AIM-9000 is comprised of an (1) IR light inlet, (2) sample stage, (3) reflective objective mirror, (4) transmission condenser mirror, (5) aperture, (6) condenser mirror (ellipsoid mirror), (7) MCT detector, (8) microscope camera, (9) wide-field camera (optional).

Fig. 1 External View of AIM-9000 IR Microscope

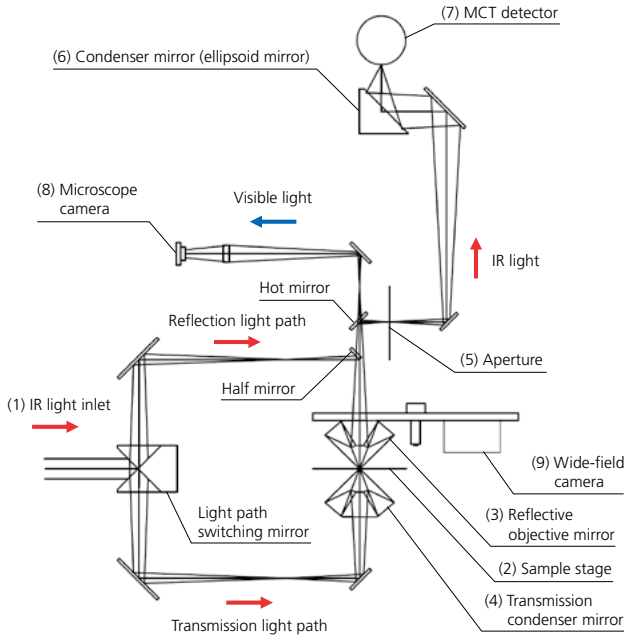

Fig. 2 Optical System in AIM-9000 IR Microscope

The individual components that comprise the AIM-9000 are described below.

(1) IR Light Inlet

The IR light used for measurement enters the AIM-9000 from an FTIR unit. A light path switching mirror directs infrared light entering the microscope either along the transmission light path or the reflection light path depending on the measurement method (transmission/reflection).

(2) Sample Stage

Used to immobilize the sample and decide where measurements are taken from the sample. The sample stage in the AIM-9000 moves in 1-µm increments in X, Y, and Z directions. The AIM-9000 also has a backlash function to ensure the positional accuracy of measurements. Various accessories can be installed on the sample stage. These include a diamond cell that applies pressure to reduce sample thickness, a micro vice holder to hold samples of various shapes in a horizontal orientation for measurement, and an ATR pressure sensor that prevents the prism from being damaged by excess pressure during ATR measurements.

(3) Reflective Objective Mirror

Fig. 3 shows the optical system of the reflective objective mirror. IR light traveling along the transmission light path follows a different path in the reflective objective mirror compared to that of IR light traveling along the reflection light path. IR light on the transmission light path transmitted by the sample passes through both sides of the reflective objective mirror and is focused at the aperture. By contrast, a half mirror reflects only half the IR light on the reflection light path into the reflective objective mirror. This IR light enters through one side of the reflective objective mirror, is reflected onto the sample surface, and IR light returning from the sample passes through the opposite side of the reflective objective mirror and is focused at the aperture. As a result, the light intensity of reflection measurements is around half that of transmission measurements. Please see FTIR TALK LETTER Vol. 29 "Objective Lenses for Infrared Microscope" for a more detailed description of the reflective objective mirror.

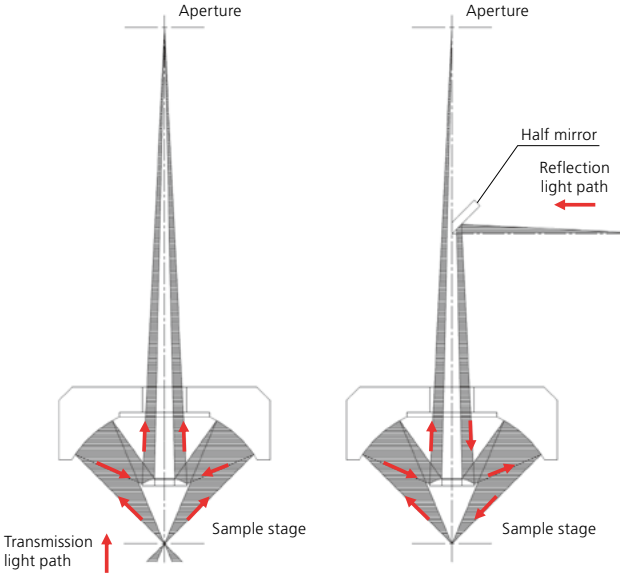

Fig. 3 Reflective Objective Mirror (Left: Transmission Light Path, Right: Reflection Light Path)

(4) Transmission Condenser Mirror

The transmission condenser mirror is located under the sample stage and focuses IR light traveling along the transmission light path onto the sample stage. When a diamond cell or a KBr or BaF_2 window plate is used, the position of the transmission condenser mirror must be adjusted to account for different refractive indices that create different focal points. AIMsolution, dedicated software for controlling the AIM-9000, has a function to automatically adjust the position of the transmission condenser mirror, making manual adjustment unnecessary. During reflection measurements, the transmission condenser mirror is not used and can be removed. AIMsolution provides information on how to remove and install the transmission condenser mirror in a navigable, conversational format that allows anyone to remove and attach the condenser mirror with ease. When the mirror is removed, samples with a maximum thickness of 40 mm can be installed and measured on the sample stage.

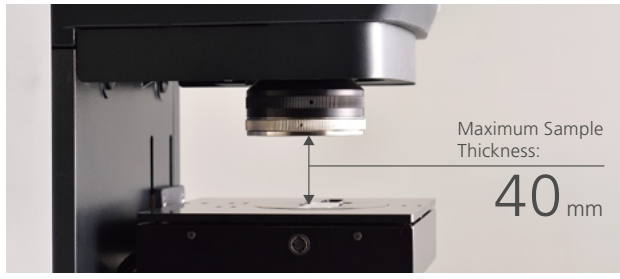

Fig. 4 Sample Stage with Condenser Mirror Removed

(5) Aperture

The size of the aperture is set to match the region intended for measurement and blocks IR light passing through other regions. Aperture size is determined by size in the X and Y directions and by rotation angle. The appropriate aperture size and angle can be set automatically using the automatic contaminant recognition system included as standard with AIMsolution. Fig. 5 shows the system used to set aperture size. The system has a "micro" setting to detect objects 10 µm and smaller and a "standard" setting to set the aperture size for larger objects. Example results from using both settings are shown. Please see FTIR TALK LETTER Vol. 28 "Infrared Microscope—Dedicated AIMsolution Software" for a more detailed description of the automatic contaminant recognition function.

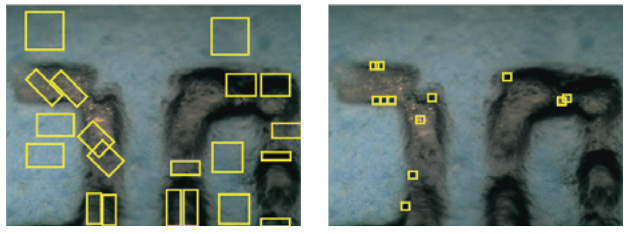

Fig. 5 Using the Automatic Contaminant Recognition Function to Set Aperture Size; Two Examples

(6) Condenser Mirror (Ellipsoid Mirror)

The condenser mirror (ellipsoid mirror) condenses IR light passing through the aperture onto the light-receiving surface of the MCT detector. Ellipsoid mirrors have two focal points and can condense IR light from one focal point onto the other focal point. Accordingly, IR light condensed at the aperture is condensed again by the condenser mirror onto the light-receiving surface of the MCT detector.

(7) MCT Detector

The MCT detector is highly sensitive and especially useful for low-light-intensity measurements, such as microscopic measurements with a microscope or analyzing gas in a gas cell with a long light path. The MCT detector is more sensitive than the tri-glycine-sulfate (TGS) detector commonly used in FTIR units and creates good spectra from only a small number of scans, but must be cooled with liquid nitrogen during operation. MCT detectors are also only capable of measuring a narrower range of wavenumbers compared to TGS detectors. In the AIM-9000, this measurable range is either 5,000 to 700 cm^{-1} (narrow band) or 5,000 to 650 cm^{-1} (middle band). Please see FTIR TALK LETTER Vol. 13 for a more detailed description of the MCT detector and FTIR TALK LETTER Vol. 12 for a more detailed description of the TGS detector.

(8) Microscope Camera

The AIM-9000 can measure IR light while also observing visible light images. A hot mirror that reflects IR light and transmits visible light is placed in the light path to simultaneously send visible light to a camera for sample observation and IR light to a detector for measurement without having to switch between visible and IR light paths. The microscope camera has a digital zoom function with a 10× maximum zoom (0.03 × 0.04 mm region).

(9) Wide-Field Camera

The wide-field camera can observe wider regions than the microscope camera. Regions 10 × 13 mm in size can be observed to quickly and easily decide where measurements are taken from the sample. The wide-field camera also has a digital zoom function that zooms to a minimum region size of 2.0 × 2.6 mm. Positional information is also shared with the microscope camera used to take IR measurements, hence the operator can switch between cameras with no positional displacement and easily switch from viewing the wide-field camera to take IR measurements with the microscope camera. Fig. 6 shows images of the surface of an electronic circuit board captured with the wide-field camera and microscope camera. The images show the 330× maximum magnification range achievable between the wide-field camera and 10× zoom on the microscope camera (0.03 × 0.04 mm). Please see FTIR TALK LETTER Vol. 27 "Infrared Microscope—Convenience of a Wide-View Camera" for a more detailed description of the functions and convenience of the wide-field camera.

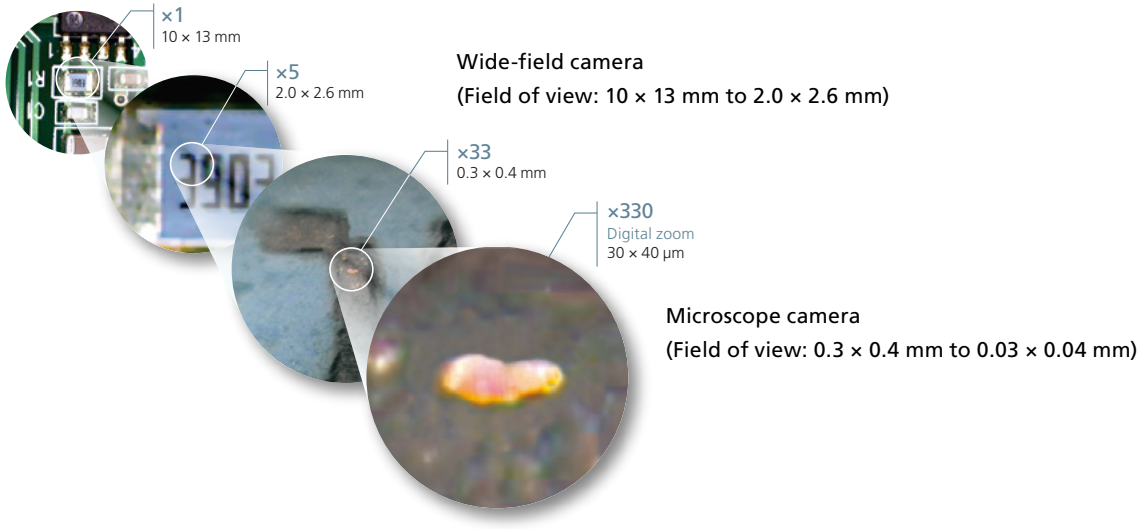

Fig. 6 Images from Wide-Field Camera and Microscope Camera

3. Summary

This article described optical systems in infrared microscopes using the Shimadzu AIM-9000 as an example. The AIM-9000 infrared microscope is equipped with many functions that are unique to Shimadzu, such as an automatic contaminant recognition system and a wide-field camera. Numerous accessories, including a visible light polarizer, IR light polarizer, ATR objective mirror, and high-sensitivity reflective objective mirror (GAO), are available for the AIM-9000 to meet a variety of different needs. Please feel free to contact Shimadzu sales representatives with inquiries.

Features of the UV-Damaged Plastics Library

Global Application Development Center, Analytical & Measuring Instruments Division
Shoko Iwasaki

The UV-Damaged Plastics Library is an original Shimadzu library of IR spectra developed to assist degradation analysis and microplastics analysis. The library was previously described in FTIR TALK LETTER Vol. 36 "Analysis of Plastic Materials Using FTIR," but this article provides more details of the features, example uses, and key points of the library.

1. Introduction

The IR spectra of plastics altered (degraded) by UV irradiation can differ from those of undegraded standard plastics and cause problems for qualitative analysis. The UV-Damaged Plastics Library enables highly accurate qualitative analysis that accounts for the degraded state of a given sample. The library can be widely used in the analysis of many types of foreign objects (in fields such as food, pharmaceutical, petroleum, and chemistry), by the contract analysis industry, and by institutes of research (microplastics analysis).

2. About the UV-Damaged Plastics Library

The library contains over 300 IR spectra from plastic samples subjected to UV irradiation collected in a database. Super accelerated weathering testers made by Iwasaki Electric Co., Ltd., shown in Fig. 1 (a) and (b), were used to prepare samples of 14 plastics with no UV light irradiation and 1 to 550-hour UV light irradiation for measuring the IR spectra.

The degradation in this library was achieved by accelerated testing with super accelerated weathering testers. To maintain uniform testing conditions, each plastic was irradiated with UV light under the same conditions (intensity: 150 mW/cm^2). Irradiation for 550 hours at an intensity of 150 mW/cm^2 in the UV light irradiation device was equivalent to approx. 10 years of outdoor exposure.

Commercially available plastic sheeting was used for plastic samples. Plastics can exhibit different changes in appearance when irradiated with UV light for an extended period, with some showing no effects and others changing color and developing a brittle surface due to degradation.

(a)

(b)

Fig. 1 Iwasaki Electric Co., Ltd. Super Accelerated Weathering Testers
(a) SUV-W161 (metal halide lamp)
(b) SUV-W262 (metal halide lamp)

This article examines changes over time of three common plastics in the UV-Damaged Plastics Library: polyethylene (PE), polypropylene (PP), and polyethylene terephthalate (PET). An example analysis of microplastics is also presented.

The IR spectra in the UV-Damaged Plastics Library were obtained using the attenuated total reflectance (ATR) technique (diamond prism). ATR obtains information from the sample surface: when a sample with a refractive index of 1.5 is analyzed with an incident angle of 45 degrees, theoretical calculations show the ATR technique collects data from ≤ 5 μm of the sample surface. ATR measurements are useful for analyzing UV degradation because UV degradation advances from the irradiated surface. A point of caution with ATR is that plastics degraded by UV light can develop a rough surface but appear normal, reducing the contact status between the sample and prism. This phenomenon can reduce the intensity of spectral peaks obtained by ATR from UV-degraded samples compared to samples with a smooth surface not irradiated

with UV light. Some of the IR spectra shown later in this article have been adjusted to compensate for this difference by matching intensity to a typical peak among reference vibrations.

3. Ultraviolet Degradation of Common Plastics

Fig. 2 shows IR spectra of PE normalized to 2,914 cm^{-1}. An absorption peak near 1,720 cm^{-1} that appears after around 100 hours of irradiation is believed to be caused by stretching vibrations of C=O groups produced by UV-induced oxidation. Ultraviolet light oxidizes the surface of PE, and PE molecule cleavage is known to be accompanied by the generation of C=O groups [1]. Another absorption peak from 1,300 to 1,000 cm^{-1} is believed to be stretching vibrations of C-O groups. The absorption peak near 3,400 cm^{-1} is also believed to be stretching vibrations of O-H groups produced by oxidation of PE.

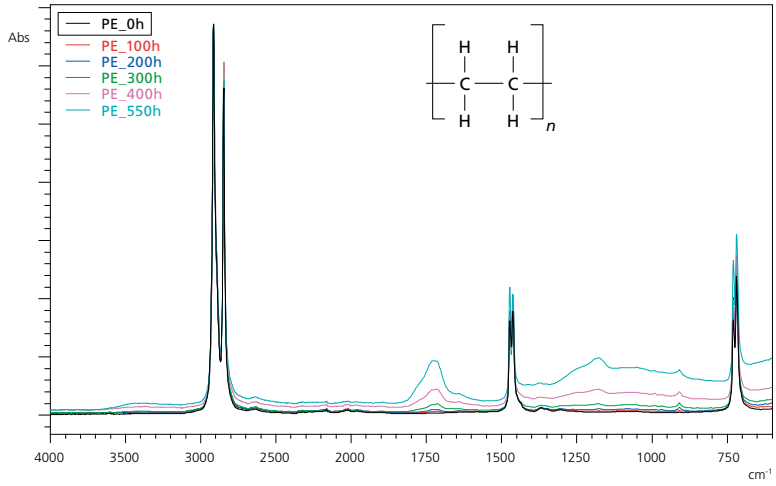

Fig. 2 IR Spectra of Polyethylene (PE)

Fig. 3 shows IR spectra of PP normalized to 2,916 cm^{-1}. An absorption peak near 1,720 cm^{-1} that appears after around 30 hours of irradiation is believed to be stretching vibrations of C=O groups produced by UV-induced oxidation. Another absorption peak from 1,300 to 1,000 cm^{-1} is believed to be stretching vibrations of C-O groups. The absorption peak near 3,400 cm^{-1} is also believed to be stretching vibrations of O-H groups produced by oxidation of PE.

Both PP and PE are polymers composed of carbon and hydrogen. Although functional groups in PP and PE undergo very similar changes upon irradiation by UV light, the changes are more marked in the IR spectra of PP.

PP is normally less weather-resistant than PE with UV degradation often posing a challenge for PP materials, and the above findings reflect this characteristic.

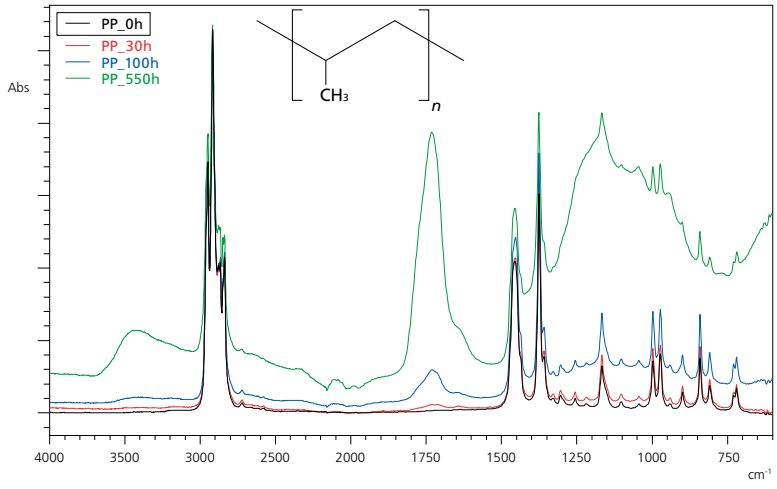

Fig. 3 IR Spectra of Polypropylene (PP)

Fig. 4 shows IR spectra of PET. The longer the duration of UV irradiation, the greater the surface degradation and the poorer the degree of contact between the plastic sample and prism, as shown by the reduced peak intensities of these spectra. After around 2 hours of UV irradiation, the C=O stretching vibration peak near 1,710 cm^{-1} and the C-O-C stretching vibration peaks near 1,240 and 1,100 cm^{-1} widen and become less acute. Note that the peak near 3,400 cm^{-1} is believed to be stretching vibrations of O-H groups produced by oxidation.

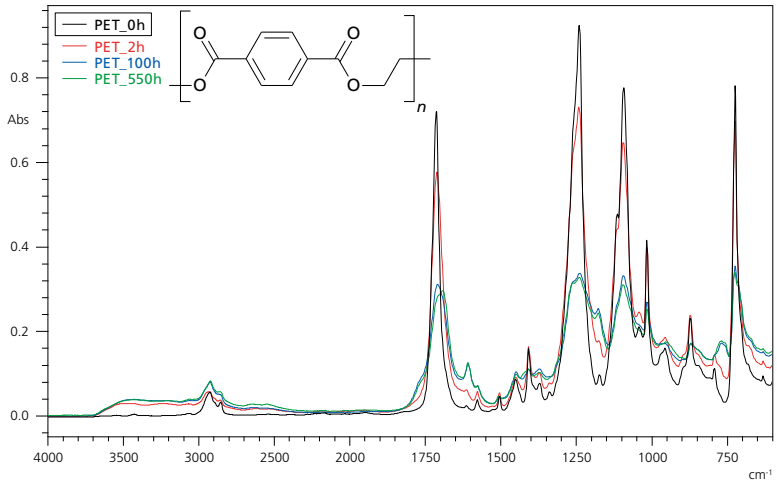

Fig. 4 IR Spectra of Polyethylene Terephthalate (PET)

4. Analysis of a Microplastic

A piece of pink plastic was analyzed from a selection of microplastics collected from the coast. The IR spectrum of the plastic and a library IR spectrum are shown in Fig. 5. The piece of pink plastic matched the IR spectrum in the UV-Damaged Plastics Library for PP irradiated with UV light for 150 hours. Based on this match, the piece of pink plastic is estimated to be PP degraded by UV-induced oxidation. Note that the wide peak from 1,200 to 900 cm^{-1} is believed to be silicate, which is used as a filler agent.

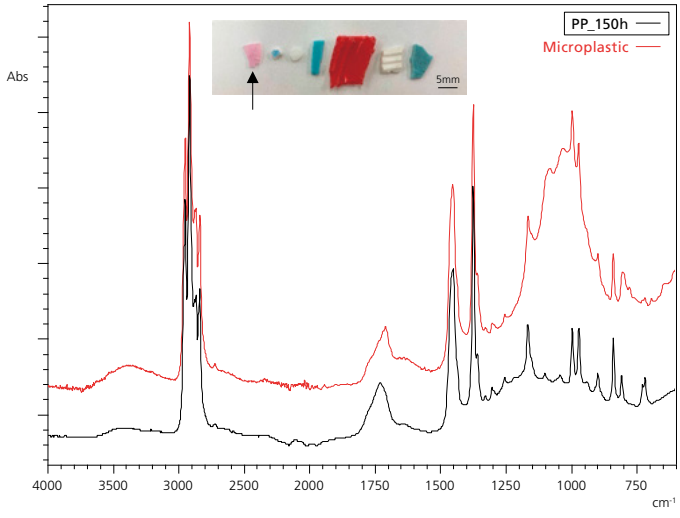

Fig. 5 Microplastic IR Spectrum

5. Key Points of the UV-Damaged Plastics Library

Although the above-mentioned features of the UV-Damaged Plastics Library are highly rated by its users, the IR spectra in the library were measured using typical commercial plastics and may differ from the IR spectra of some products. For example, the antioxidant content of plastic may affect the degree of degradation caused by a given duration of UV irradiation. Degradation by UV light can also deposit additives on the surface of plastics. Caution is even needed in cases of an almost exact spectral match as the samples used to create these library spectra were not exposed to the effects of rainfall and other natural phenomena; hence, they cannot be used to calculate the duration of weather exposure.

6. Summary

Degradation changes the IR spectral shape of plastics. As a result, degraded plastics do not match exactly with IR spectral libraries that are created from standard materials and can be difficult to identify. In such cases, an IR spectral library of ultraviolet-damaged plastics, such as the one described in this article, can enable more accurate identification of a given plastic (though only if the material to be identified is included in the UV-Damaged Plastics Library).

Workability, recyclability, and long-term durability are among the characteristics required of plastics today, and plastic products necessitate the development of highly functional additives that prevent degradation [1]. Shimadzu hopes the UV-Damaged Plastics Library featured in this article and developed to assist degradation analysis and microplastics analysis will find use in a wide range of applications.

Shimadzu also produces a counterpart product in its Thermal-Damaged Plastics Library. The Thermal-Damaged Plastics Library collects absorption spectra from 13 plastics oxidized by heating and is useful for analyzing foreign objects or other unknown samples and defective products affected by heat during the manufacturing process.

Shimadzu also sells the "Plastic Analyzer," which combines these two degraded plastics libraries with the Shimadzu IRSpirit compact FTIR spectrophotometer.

Please contact Shimadzu representatives to learn more about solutions for analysis of degraded plastics.

References

[1] Nishioka T. and Housaki T. (Eds). A Guide on Plastic Analysis. Maruzen Publishing (2011) [in Japanese]

The Questions and Answers section has been omitted from this issue due to the circumstances of publication.

— To Customers Using Shimadzu Fourier Transform Infrared Spectrophotometers —

Supply of Spare Parts for FTIR-8000 Series/IRPrestige-21 has Ended

Thank you for your continued use and enjoyment of Shimadzu Fourier Transform Infrared Spectrophotometers.
Shimadzu has strived daily to supply spare parts for the FTIR-8000 Series/IRPrestige-21 even after ending production of these models, but continuing to supply these spare parts has now become impractical.
This may cause circumstances where repair is impossible and may have a significant bearing on your analysis work.
Please consider upgrading to a new Fourier Transform Infrared Spectrophotometer.

Consider Upgrading to the Latest Models!

IRTracer-100
High-sensitivity, high-resolution, and high-speed measurements

IRAffinity-1S
High-sensitivity, high-resolution, and reduced maintenance

IRSpirit
Compact design and highly expandable

IRPrestige-21
Production of this model ended in 2013

IRPrestige-21
Production of this model ended in 2008

FTIR-8000 Series

Learn more about our current FTIR models

SHIMADZU

Shimadzu Corporation
www.shimadzu.com/an/